Sensors & Diagnostics

ROYAL SOCIETY OF CHEMISTRY

PAPER

View Article Online
View Journal

Check for updates

Cite this: DOI: 10.1039/d6sd00016a

Received 21st January 2026,
Accepted 22nd March 2026

DOI: 10.1039/d6sd00016a

rsc.li/sensors

Measurement-aligned finite element modeling for predictive design of dual-port SAW resonators

Hongyang Guo,[a] Xiaojing Zhang,[a] Xinxin Li,[b] Ping Wang,*[ac]
Hao Jia*[b] and Liujing Zhuang*[a]

Surface acoustic wave (SAW) resonators are attractive building blocks for biomimetic olfaction and gustation arrays because their narrowband spectral features support sensitive resonance tracking. However, key metrics such as quality factor (Q) and ripple are highly sensitive to modeling assumptions and to the external measurement chain, which often leads to a gap between idealized simulations and experimental spectra. Here we present a measurement-aligned finite element method (MA-FEM) workflow for dual-port resonant Rayleigh-wave SAW devices that systematically drives the model toward real operating behavior. The approach combines stable domain and meshing settings, physically constrained loss calibration, and compact lumped element loading to capture dominant parasitic effects. Using the validated model, we perform parameter sweeps and build "the number of interdigital transducer (IDT) electrode pairs (N_1) and reflector strips (N_2) to Q" design maps that provide actionable selection windows and reveal high Q solutions under footprint constraints through trade-offs between transduction strength and cavity feedback. This work offers a reproducible simulation driven route to reduce fabrication trial and error and to support array-oriented SAW sensor design.

1. Introduction

Biomimetic olfaction sensing systems, commonly known as electronic noses, rely on cross-sensitive multi-sensor arrays coupled with pattern-recognition algorithms to emulate biological chemosensory functions.[1,2] As a crucial frontend platform for implementing such biomimetic arrays, surface acoustic wave (SAW) devices have attracted significant attention due to their high operating frequency, capability of achieving high quality factors (Q),[3] strong sensitivity to interfacial mass loading and viscoelastic perturbations,[4] and compatibility with array integration.[5] In particular, resonant SAW devices provide narrowband resonances and steep phase responses, enabling weak perturbations to be transduced into measurable shifts in center frequency or phase. This feature offers high-resolution, low-noise primitive signals that are advantageous for pattern-recognition-centric biomimetic systems.[6]

However, some engineering challenges have hindered the large-scale manufacturing and application of SAW devices. For instance, environmental temperature and packaging conditions can lead to drift phenomena,[7] where multipath reflections and parasitic modes within the device cause fluctuations in peak shape and spurious peaks,[8,9] as well as differences in the initial resonant frequency and response consistency between different channels due to manufacturing tolerances and uneven coating.[10] Traditional SAW design methodologies frequently rely on analytical models, standard equivalent-circuit models (ECM), or idealized finite element method (FEM) simulations.[11] Such approaches are effective for preliminary estimation and trend analysis. While useful for preliminary estimation, these approaches often lack geometric causality and struggle to capture the multi-physics coupling and external parasitic interferences in a unified manner. Consequently, engineering optimization still commonly proceeds *via* a trial-and-error loop of fabrication–measurement–refabrication, which severely hinders the large-scale development of biomimetic arrays.

To address this gap, we propose a measurement-aligned finite element method (MA-FEM) to establish an electro-acoustic model for dual-port resonant Rayleigh-wave SAW devices that couples piezoelectric–structural dynamics with electrical terminals and a compact external loading network. The workflow is organized as engineering-reproducible steps that stabilize numerical behavior and incorporate effective loss and external loading, so that the simulated peak envelope, ripple trend, bandwidth, and Q follow measured

---

[a] *Biosensor National Special Laboratory, Key Laboratory of Biomedical Engineering of Education Ministry, Zhejiang Key Laboratory of Intelligent Sensing Technology and Advanced Medical Instrument, Zhejiang University, Hangzhou, China. E-mail: zhuangliujing@zju.edu.cn*
[b] *State Key Laboratory of Transducer Technology, Shanghai Institute of Microsystem and Information Technology, Chinese Academy of Sciences, Shanghai, China*
[c] *Binjiang Research Institute, Zhejiang University, Hangzhou, China*

magnitudes and tendencies. Although studies of SAW sensors for gas and biochemical detection and array recognition are abundant,[12–14] the engineering-oriented SAW simulation methodology is often dispersed across implementation details.

By stabilizing numerical boundaries and resolving electrode-scale meshing, the MA-FEM precisely aligns simulated peak envelopes, ripple trends, and Q factors with vector network analyzer (VNA) measurements. Building on this validated model, we perform extensive structural parameter sweeps to construct actionable design maps (linking the number of interdigital pairs N_1, reflector strips N_1, to the overall Q). This work provides a computationally robust and experimentally validated framework. It shifts the paradigm from empirical trial-and-error to simulation-driven predictive design, laying a reliable methodological groundwork for the digital-twin-assisted optimization of smart SAW olfaction sensor arrays.

2. Device architecture and design parameters

2.1 Piezoelectric substrate and operating mode

The overall performance of a resonant SAW device is strongly tied to the wave-propagation and loss characteristics of the piezoelectric substrate. Before discussing geometric modeling, it is useful to clarify which substrate-related quantities set the operating scale and how they affect resonance sharpness and spectral stability.

In SAW resonators, the surface-wave phase velocity (v) determines the wavelength (λ) at a target center frequency (f_0) through ($\lambda = v/f_0$), and therefore constrains the IDT periodicity and feature sizes. As the operating frequency increases, the characteristic dimensions shrink, which tightens lithography tolerances and makes the response more sensitive to practical non-idealities. In addition, high frequency resonant devices tend to be more susceptible to boundary reflections, numerical dispersion, and parasitic loading, which often manifest as peak-shape distortion or enhanced ripple if not properly controlled. The electromechanical coupling coefficient (K^2) sets the baseline conversion efficiency between electrical and acoustic energy and is closely related to achievable insertion loss. However, in real resonators the peak shape and the Q factor are also influenced by energy dissipation in the substrate and surrounding structures, scattering at electrode features, absorption at boundaries, and impedance loading introduced by the measurement chain. Temperature effects are equally difficult to ignore in array settings. Even modest environmental changes can shift the resonance frequency, complicate baseline correction, and reduce the portability of a trained classifier. Finally, dielectric properties and electrode–substrate capacitance modulate the effective port impedance and can amplify or mitigate how external interconnects and packaging parasitics affect the peak depth, bandwidth, and phase slope at high frequency.[15]

To provide context for substrate selection in SAW device design, Table 1 summarizes representative Rayleigh-mode SAW-relevant properties of several commonly used piezoelectric crystals, including the SAW phase velocity, the K^2, the temperature coefficient of frequency (TCF), and the relative permittivity (ε_r). These parameters jointly affect the attainable operating frequency, transduction efficiency, thermal drift, and electrical loading associated with the IDT capacitance. Because these quantities are generally cut- and propagation-direction-dependent and may vary with the adopted definitions, the values in Table 1 are intended as indicative benchmarks rather than absolute constants.

2.2 IDTs and reflector gratings

As shown in Fig. 1, the dual-port SAW resonator consists of an input/output pair of interdigital transducers (IDTs) and two reflector gratings that form an acoustic cavity. The input IDT will convert the applied signal in the MHz or GHz frequency range into surface acoustic waves that propagate along the surface of the piezoelectric substrate, and the reflector gratings provide acoustic feedback so that multiple round trips build up a resonance condition in the cavity. The output IDT reconverts the acoustic wave into an electrical signal, enabling standard scattering parameters *via* transmission responses.[19] Throughout this work, the Rayleigh-wave wavelength is denoted as λ, set by the IDT periodicity and the target operating frequency.

Each IDT is described by its period λ (or pitch), electrode width a, electrode gap b, metallization ratio $a/(a + b)$, aperture W, and electrode thickness h. The W defines the overlap length of the interdigitated electrodes and thus sets the effective acoustic beam width and active transduction area. For different types of surface acoustic wave sensors, the

Table 1 Representative properties of piezoelectric substrates for SAW devices[16–18]

Substrate	Cut/propagation	Velocity (m s^{-1})	K^2(%)	TCF (ppm °C^{-1})	ε_r
Quartz	ST, X	3158	0.16	Nonlinear	4.55
Quartz	AT, X	3159	0.23	Nonlinear	4.52
$LiNbO_3$	Y, Z	3488	4.5	−87	50.2
$LiNbO_3$	128° YX	3975	5.5	75	85
$LiTaO_3$	36° YX	4212	2.2	45	47
$LiTaO_3$	Y, Z	3230	0.74	−31	47.9
$Bi_{12}GeO_{20}$	100 011	1681	1.2	−122	38

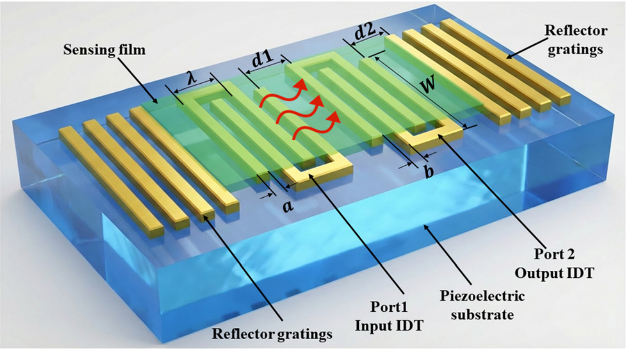

Fig. 1 Schematic of the dual-port SAW resonator.

Table 2 Design parameters of a dual-port resonant SAW device

Parameter	Symbol	Value/notes
Piezoelectric substrate	—	ST-cut quartz
Electrode material	—	Au
Metallization ratio	—	50%
Electrode thickness	h	100 nm
Resonant frequency	f_0	263 MHz
Number of electrode pairs (per IDT)	N_1	50
Number of reflector strips (per side)	N_2	350
Aperture	W	800um
Acoustic wavelength/IDT period	λ	12um
Electrode width	a	$\lambda/4$
Electrode gap	b	$\lambda/4$
IDT–IDT gap	d_1	λ
Reflector–IDT gap	d_2	1.25λ

optimal aperture size is also different.[20] W affects the overall acoustic energy conduction and power-handling capacity, and it also influences diffraction-induced beam spreading and edge scattering. A wider-aperture IDT generally excites SAWs with higher amplitude and thus yields lower insertion loss, while the increased aperture also raises the IDT's equivalent capacitance, which can degrade high frequency signal transmission in the device. The metallization ratio is fixed at 0.5 unless otherwise stated, which typically yields efficient excitation of the intended fundamental SAW mode while suppressing unwanted even-harmonic content and reducing geometric bias in the transduction pattern.[21] To avoid introducing excessive degrees of freedom, λ, metallization ratio, W, and h are kept constant in this study, while N_1 is treated as one of the primary structural variables because it directly modifies the effective transduction strength and therefore impacts resonance sharpness and susceptibility to parasitic features. Each reflector grating is characterized by its strip count N_2, reflector pitch, duty ratio, and thickness. The reflector pitch is selected close to $\lambda/2$ to satisfy the Bragg condition and maximize reflection around the target frequency, while the duty ratio and thickness are held constant during the main sweeps to isolate the effects of N_2 and cavity geometry.[22] In addition to N_2, the reflector–IDT spacing is a key cavity parameter that strongly affects ripple and the apparent Q through interference between the acoustic path and residual electrical feedthrough. The spacing parameter d_2 is defined using the first reflector strip adjacent to the IDT. Specifically, d_2 is referenced to the midpoint of the gap between that first reflector strip and the nearest IDT electrode, which provides a consistent geometric definition across the parameter space.

With these definitions, the subsequent results focus on how N_1, N_2, and d jointly shape Q and ripple trends under the measurement-aligned modeling workflow, and how trade-offs can be made when footprint constraints limit the available IDT length or reflector length. Table 2 summarizes the key design parameters used throughout this study and serves as a unified reference for the geometry and material assumptions adopted in the subsequent analyses.

In biomimetic olfaction and gas sensing systems, the surface of a SAW device is frequently coated with a sensing film to act as a chemical receptor for specific volatile organic compounds (VOCs).[23] Upon adsorbing target gas molecules, the sensing film undergoes significant mass loading and viscoelastic perturbations that alter acoustic wave propagation, which serves as a primary physical mechanism for high sensitivity detection. However, the inherent viscoelasticity of polymer coatings exacerbates wave attenuation and acoustic energy dissipation, directly leading to a degraded overall Q and increased insertion loss.[24,25]

It is worth noting that applying a chemical sensing film is not the only paradigm for SAW-based olfaction. In gas chromatography-surface acoustic wave (GC-SAW) systems, target gases are physically separated by an upstream capillary column, allowing an uncoated bare SAW resonator to be utilized purely as an ultra-sensitive mass detector without requiring specific chemical functionalization.[26]

Consequently, given the diverse physical properties of various sensing films and the alternative bare-probe applications, embedding specific film parameters into the MA-FEM sweeps would introduce excessive variables and obscure the intrinsic acoustic scaling laws. Thus, we deliberately excluded the sensing film during structural simulations to focus exclusively on maximizing the initial Q of the bare cavity. Establishing this robust high Q baseline is a fundamental prerequisite to ensure a sharp spectral response, regardless of subsequent polymer damping or bare operation.

3. Implementation of the MA-FEM workflow

For resonant SAW devices, the quality factor and ripple are highly sensitive to numerical implementation. Boundary reflections, mesh dispersion, and idealized port conditions can distort the S_{21} spectrum and lead to unrealistic Q or spurious features. The modeling strategy therefore follows a progressive alignment principle. Numerical stability and repeatability are established first, then physically motivated loss and electrical loading are introduced so that the simulated spectra follow measurement in trend and order of magnitude for the key observables.

3.1 Computational domain and absorbing boundaries

The model explicitly includes, in the vertical direction, the piezoelectric substrate, the electrodes, and an air domain above the device. Introducing the air domain serves two main purposes. First, the SAW displacement field exhibits a pronounced out-of-plane component and a near-field distribution in the vicinity of the surface. If the region above the surface is simplified as a truncated boundary, it can easily impose non-physical constraints and induce artificial reflections near the surface. Second, at high frequencies, energy leakage and the treatment of boundary conditions in the near-surface region can affect the resonance bandwidth and peak-shape details. Including an air domain helps the top boundary better approximate the practical "free-surface" operating condition.

The characteristic thickness of the air domain can be related to the Stokes boundary-layer thickness,

$$\delta = \sqrt{\frac{2\nu}{\omega}} \tag{1}$$

where ν is the kinematic viscosity of the medium and ω is the angular frequency.[27] This length scale reflects the primary normal-direction decay range of near-field viscous shear/velocity perturbations driven by an oscillating interface. Therefore, in frequency-domain electro–acoustic simulations, the air-domain height should cover at least several times δ to ensure that the upper boundary does not introduce additional constraints or reflections to the near-surface displacement/stress fields. Since δ at the operating frequency is typically much smaller than the acoustic wavelength λ, and to maintain a consistent geometric scaling across the structural parameter sweep while controlling the computational cost, we set the air-domain height to $h \approx 1.5\lambda$, thereby ensuring $h \gg \delta$.

Perfectly matched layers are applied on the lateral sides and the bottom boundary to absorb outward-propagating elastic waves and suppress boundary reflections. The PML thickness is scaled with lambda to preserve absorption effectiveness across different structural parameters without excessive computational cost. A low-reflection open boundary condition is used at the top of the air domain to avoid additional constraints on the surface field. A stability check is performed by enlarging the air domain or thickening the PML while keeping all other settings unchanged, then confirming that f_0, Q, and the ripple metric vary only marginally. Once these indicators stabilize, subsequent mesh refinement and loss calibration become meaningful.

3.2 Electrode resolved meshing and convergence

The second major factor controlling the fidelity of a SAW resonance simulation is mesh resolution, especially around the electrode features. Since the IDTs and reflectors are responsible for wave excitation, scattering, and cavity formation, insufficient resolution at electrode edges can introduce numerical dispersion and artificial loss, which typically shows up as underestimated Q or distorted peak shapes. Meanwhile, using a uniformly fine mesh across the entire domain is computationally inefficient and often impractical for large sweeps. We therefore adopt a hybrid meshing strategy that resolves electrode-scale physics while keeping the overall mesh size manageable.

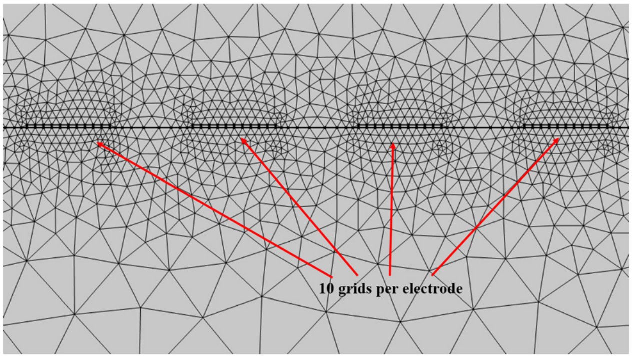

Fig. 2 Cross-sectional mesh density distribution of the SAW resonator model.

Specifically, we apply a structured (mapped) mesh in the electrode regions and enforce a minimum resolution along the electrode width direction. In our baseline configuration, each electrode width is approximately evenly divided into 10 grids, which means that each electrode is analyzed ten times during frequency domain analysis. Outside the electrode area, the remaining geometries are meshed using unstructured free triangular grids, thereby balancing high-fidelity physics with computational tractability during large-scale parametric sweeps (Fig. 2).

3.3 Loss modeling in piezoelectric and elastic domains

Even with stable boundaries and a converged mesh, an ideal lossless model typically produces unrealistically high Q and overly sharp resonance peaks compared with experimental spectra. In practical SAW devices, energy is dissipated through intrinsic material damping, dielectric loss, electrode-related scattering, and coupling to surrounding media. To bring the simulated bandwidth and peak envelope into a realistic range, effective loss mechanisms are introduced in both the piezoelectric and elastic domains.

Under the structural-damping assumption, material loss is introduced by allowing the stiffness to be complex. Specifically, we write the effective Young's modulus as

$$E^{*} = E'(1 + j\eta_{\mathrm{eff}}) \tag{2}$$

where η_{eff} is the loss factor. For lightly damped resonances, η is closely linked to the observed resonance linewidth. The Q can be obtained from the half-power bandwidth as

$$Q = \frac{f_0}{\Delta f} \tag{3}$$

where Δf is the −3 dB bandwidth. For a lightly damped acoustic resonator, this macroscopic bandwidth metric establishes a direct theoretical boundary for the effective structural loss factor (η_{eff}), governed by the analytical relationship:[28]

$$\eta_{\text{eff}} \approx \frac{1}{Q} = \frac{\Delta f}{f_0} \tag{4}$$

It is important to clarify that the incorporated loss factors η_{piezo} and η_{elastic} are treated as effective phenomenological fitting parameters constrained by this theoretical basis.[29] In practical SAW devices, energy dissipation stems from a complex amalgamation of intrinsic quartz damping, acoustic scattering at the electrode features, and bulk acoustic wave leakage into the substrate.[8] When separate loss factors are assigned to the piezoelectric substrate and to linear elastic structural domains, η_{eff} can be interpreted as an energy-weighted combination of their contributions.[30] After calibration at the nominal point, the loss settings are held fixed throughout the parametric sweep to preserve comparability of Q and ripple trends.

Through a step-by-step iterative approximation, these effective values ($\eta_{\text{piezo}} = 2\text{e}^{-4}$ and $\eta_{\text{elastic}} = 5\text{e}^{-3}$) were determined by precisely matching the simulated −3 dB bandwidth with the experimentally observed linewidth at the nominal design point. To ensure the physical validity of applying these fixed effective loss factors across the entire design sweep, all experimental validations were strictly conducted using ST-cut quartz wafers from the identical manufacturing batch. It is crucial to note that within the MA-FEM framework, η_{piezo} and η_{elastic} serve as unit-volume material and interfacial loss coefficients rather than lumped total device losses. Throughout the parametric sweeps of N_1 and N_2, the local unit-cell geometry—specifically the wavelength λ, electrode thickness h, and metallization ratio—remains strictly invariant. Consequently, the fundamental wave scattering physics per electrode and the intrinsic attenuation per unit volume of quartz are assumed constant. Because the FEM spatially resolves the exact geometric count of the IDT pairs and reflectors, the macroscopic scaling of total energy dissipation (*e.g.*, increased total scattering in a longer IDT array) is inherently captured by the solver's spatial integration over the expanded domain. Therefore, holding the phenomenological loss parameters fixed after the nominal point calibration is a physically consistent strategy that naturally preserves geometric causality across the array-oriented design maps.

3.4 External circuit loading for measurement alignment

Experimental S_{21} spectra are shaped not only by the device but also by the measurement chain. Pads, interconnects, probe contacts, cable parasitics, and port mismatch can effectively load the IDT terminals and alter peak depth, baseline level, and apparent bandwidth. If the simulation assumes ideal 50 Ω terminations without parasitic effects, systematic offsets in insertion loss and peak symmetry may remain even when the internal device model is stable and includes effective loss.

To account for these effects, some studies employ established calibration strategies from microwave engineering to represent the transition from the IDT terminals to the measurement reference plane.[31] In this work, we adopt a compact lumped element loading network strictly as an engineering surrogate for the external measurement chain (*i.e.*, pads, wire bonds, and probing contacts). Unlike conventional equivalent-circuit calibration that mathematically replaces the entire acoustic device with fitted RC parameters, our approach explicitly decouples the external parasitics from the internal device physics. As shown in Fig. 3a, the dual-port SAW resonator block remains a fully meshed physical FEM domain, while it is connected to the external lumped network and nominal 50 Ω source/load ports. This architectural separation ensures that the internal electro-acoustic scattering physics responds causally to geometric modifications, while the external network accurately captures baseline offsets and feedthrough interference typically observed in practical VNA measurements. Fig. 3b shows the impact of sweeping C_{feed} over a physically reasonable range. Increasing C_{feed} systematically raises the transmission baseline and strengthens feedthrough interference with the acoustic path, which in turn modifies the peak envelope and increases ripple in the vicinity of the main resonance. Fig. 3c isolates the influence of symmetric series loss by setting $R1$ equal to $R2$. In this case, the primary effect is a change in the overall insertion loss level and peak depth, while the resonance position and the local ripple pattern remain comparatively less affected, consistent with an attenuation dominated mechanism. Fig. 3d examines variations in R_{load}. As the termination deviates from 50 Ω, the ripple amplitude and peak shape become more sensitive, reflecting mismatch induced reflections and interference that can distort the measured spectrum.

To ensure full transparency and reproducibility of the MA-FEM workflow, the specific values of the lumped elements extracted for the nominal measurement chain are disclosed. The VNA ports are modeled with the standard source and load impedance of 50 Ω. The parasitic effects introduced by the measurement fixture (*e.g.*, probing contacts and wire bonds) are represented by a symmetric series resistance $R1 = R2 = 3\ \Omega$. The coupling to the ground plane is modeled by a substrate leakage resistance R_{load} (typically ≥ 10 kΩ for a highly insulating baseline, but explicitly swept in Fig. 3d to analyze mismatch effects). Furthermore, the electromagnetic crosstalk across the test board is captured by a feedthrough capacitance $C_{\text{feed}} = 8$ fF. These parameters were kept strictly constant throughout all subsequent parametric sweeps, ensuring that any spectral variations are causally driven solely by the acoustic geometry.

3.5 Frequency sweep strategy and metric extraction

To accurately extract f_0, Q and ripple from the transmission characteristic curve, it is necessary to strictly control the step size of the frequency domain analysis. If the step size of the frequency domain analysis is too large, it may lead to

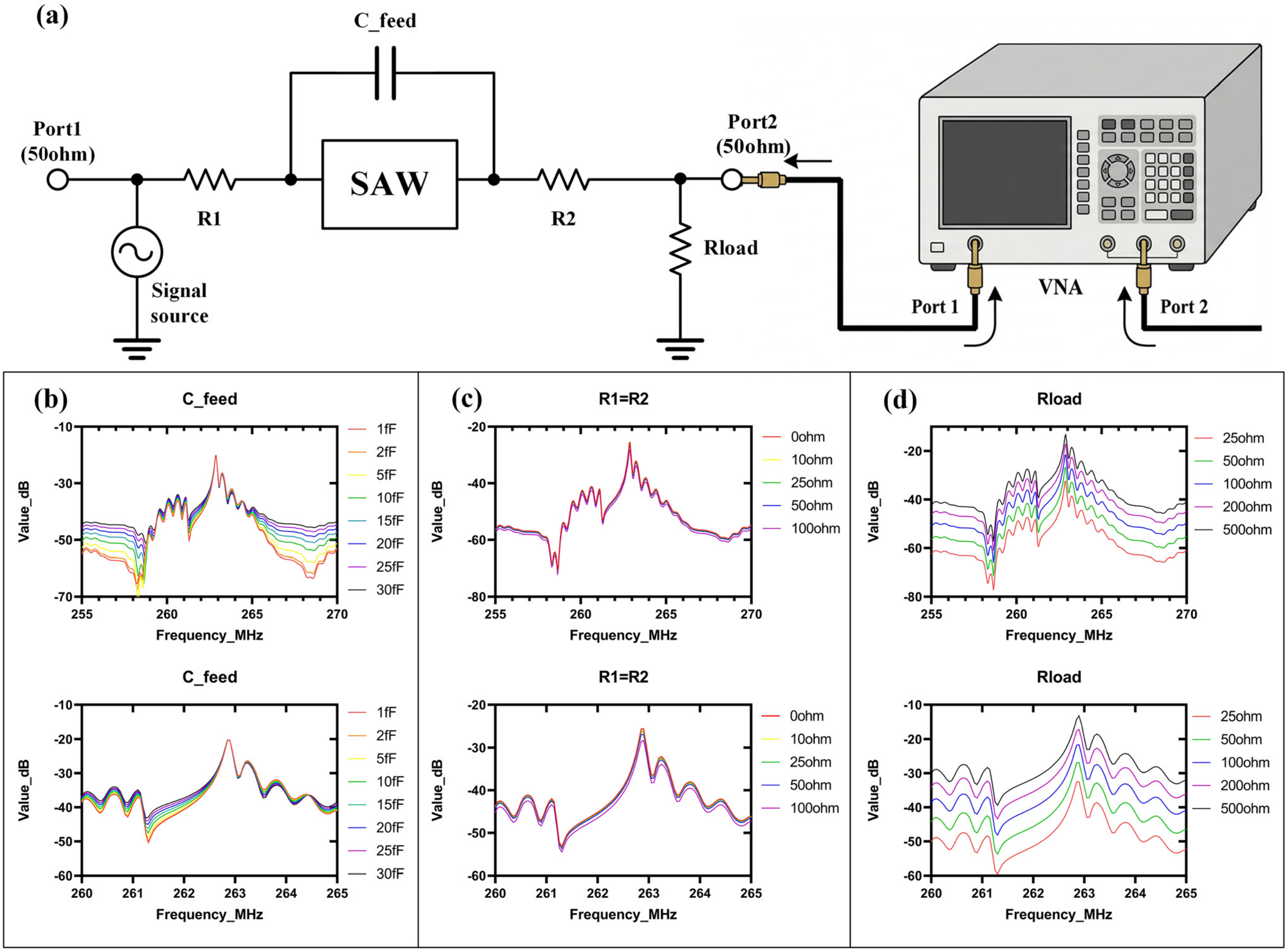

Fig. 3 Measurement-aligned lumped element loading model and its impact on the simulated S_{21} response. (a) VNA-based test circuit topology. Effects of varying (b) feedthrough capacitance C_{feed}, (c) series resistance $R1 = R2$, and (d) load resistance R_{load} on the transmission characteristics (top row: wideband view; bottom row: narrowband view).

quantization errors in the bandwidth estimation. If the step size is too small, it will result in excessive simulation calculations, which is not conducive to parameter scanning and data analysis. This problem is particularly severe for resonances with high Q values, because the −3 dB bandwidth may be narrower compared to the typical scanning step size used for low Q value devices.

In detail, we recommend defining sweep settings using a bandwidth resolution criterion and validating them by step size refinement. In practice, the step size should be sufficiently smaller than the minus 3 dB bandwidth Δf so that each linewidth contains adequate sampling points, a practical rule is 10 to 20 points within Δf

$$\Delta f_{\text{step}} \leq \frac{\Delta f}{10 \text{ to } 20} \tag{5}$$

$$\Delta f \approx \frac{f_0}{Q} \tag{6}$$

To balance accuracy and computational cost for large parametric studies, a staged sweep is preferred. A coarse sweep over a wide span localizes the resonance region and provides an initial estimate of f_0. A fine sweep within a narrow window centered at f_0 then resolves the half-power crossings and ripple structure. A practical guideline is to ensure at least ten to twenty frequency points within the linewidth Δf so that the extracted Q and ripple metrics remain stable under step refinement. The resonant frequency f_0 is defined as the frequency at maximum S_{21} magnitude. Ripple is quantified using a dedicated ripple index within a fixed window around the main resonance, enabling consistent comparison across large parametric datasets through automated post-processing.

4. Results and discussion

4.1 Experimental validation and baseline spectral comparison

To verify device measurability under a realistic measurement chain and to capture the representative spectral features, the packaged dual-port resonant SAW chip was mounted on a custom test board and characterized using a VNA-E5071C, as

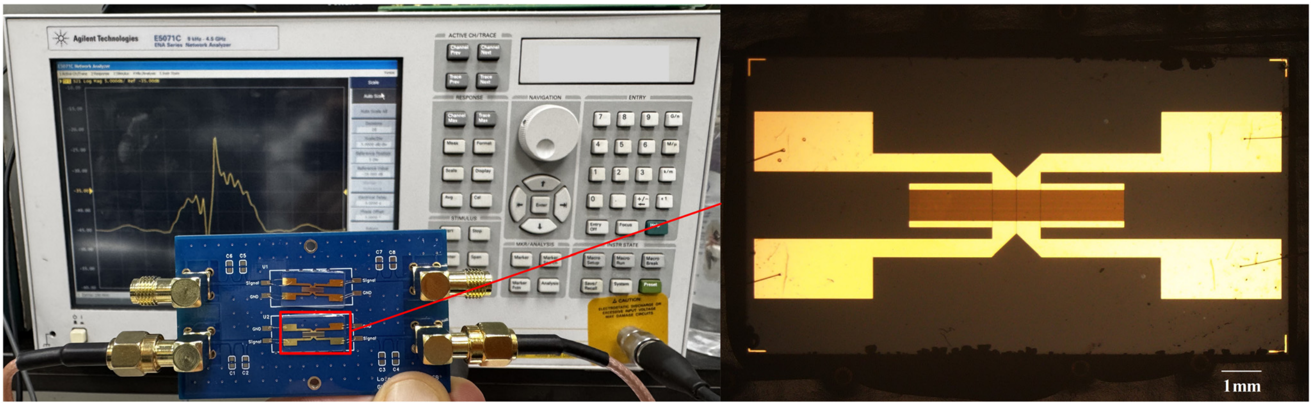

Fig. 4 Photographs of the measurement setup and the fabricated dual port resonant SAW device.

shown in Fig. 4. The left image shows the chip mounted on a custom test board with coaxial connections during VNA characterization while the right image shows an optical micrograph of the fabricated device layout, where the chip electrodes are connected to the board pads by gold wire bonding. Electrical connection between the chip electrodes and the board pads was implemented by gold wire bonding. Because this bonding and packaging approach introduces non-negligible parasitic inductance and capacitance as well as contact related loss, the subsequent modeling incorporates port impedance and external circuit loading to improve the agreement between simulated and measured spectra in terms of peak depth, bandwidth, and baseline behavior.

The comparison is shown in Fig. 5. The red trace shows the S_{21} magnitude measured by a VNA-E5071C, while the blue trace shows the S_{21} magnitude predicted by the FEM model under the same nominal design and loading assumptions. The black trace reports the residual, defined as S_{21} measured minus S_{21} simulated, with the dotted line indicating zero residual. The simulated and measured transmission responses exhibit consistent resonance behavior at the level of the main spectral envelope. In particular, the dominant resonance is aligned at approximately 262.9 MHz in both traces, and the peak magnitude agrees within about 0.2 dB. Away from resonance, the off-resonance baseline shows an offset of roughly 0.9 dB, which is consistent with the practical uncertainty associated with fixture loss, port referencing, and residual parasitics introduced by coaxial connections and wire bonding. The measured Q is on the order of 1.7×10^3, whereas the model yields about 1.4×10^3. This difference suggests that, while the dominant loading and dissipation mechanisms are captured at an effective level, additional loss and parasitic pathways that are difficult to parameterize explicitly, such as bonding-related inductance, contact-related loss, electrode scattering, and microscopic fabrication variations, can still broaden the measured resonance. Overall, the agreement in resonance frequency, peak envelope, and baseline trend supports that the proposed modeling workflow is sufficiently accurate for design screening and for extracting consistent Q and ripple trends in large parametric sweeps, rather than targeting a point-by-point reproduction of every ripple detail.

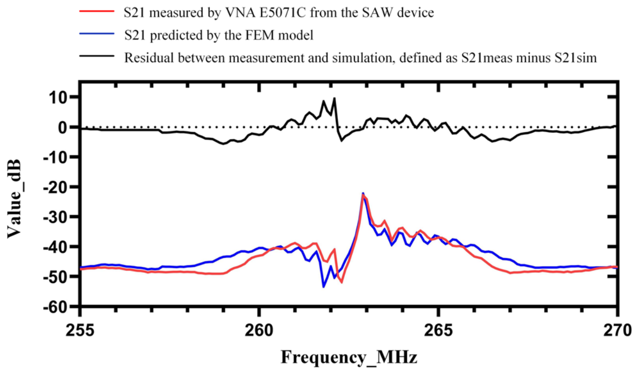

Fig. 5 Comparison between the measured and simulated transmission responses of the dual-port resonant SAW device over 255 to 270 MHz.

4.2 Quantitative benchmarking against conventional modeling approaches

To clarify the necessity and predictive advantage of the proposed MA-FEM workflow, a quantitative benchmarking analysis was performed against conventional modeling paradigms commonly utilized in SAW device design: an idealized "bare" FEM, an equivalent-circuit model (ECM), and the coupling-of-modes (COM) theory, which is shown in Table 3.

While conventional approaches are effective for preliminary estimations, they frequently fall short of capturing multi-physics coupling and impedance loading in a unified, predictive manner. For instance, standard 1D COM models require extensive empirical parameter extraction—often necessitating prior FEM dispersive curve calculations—and inherently struggle to account for 3D parasitic modes and substrate leakage.[32,33] Similarly, while the ECM can perfectly match the experimental S_{21} spectrum of a pre-fabricated device by tuning RLC values, it fundamentally lacks geometric causality; it cannot inherently predict spectral changes when structural parameters are modified without relying on newly extracted empirical data from fabricated test structures.[34,35] Furthermore, an idealized FEM without external circuit considerations severely overestimates the Q and fails to capture the asymmetric baseline offset induced by actual measurement chains.[36]

Table 3 Quantitative performance comparison of different modeling approaches for the nominal SAW resonator

Modeling approach	Q	Q error *vs.* Exp.	Baseline offset capability	Geometric causality[a]
Experimental	$\sim 1.7 \times 10^3$	N/A	Observed (∼−0.9 dB)	N/A
MA-FEM	$\sim 1.4 \times 10^3$	−17.6%	Yes (captured)	Yes
Bare FEM	Over 10^4	Over +400%	No (0 dB, symmetric)	Yes
ECM	$\sim 1.7 \times 10^3$	∼0% (forced fit)	Yes (forced fit)	No
1D COM theory	2.5×10^3	Moderate	No (misses parasitics)	Limited

[a] Geometric causality indicates whether the model can inherently predict spectral changes when structural parameters (*e.g.*, N_1, N_2) are modified, without requiring new empirical data extraction from newly fabricated test structures.

The proposed MA-FEM successfully bridges this critical gap. By yielding a predicted Q of 1.4×10^3 (an acceptable engineering margin of −23.5% error) and accurately capturing the baseline offset, the MA-FEM demonstrates a robust balance between physical rigorousness and measurement reality. Crucially, unlike the ECM, the MA-FEM retains strict geometric causality. The phenomenological loss parameters calibrated at the nominal point remain fixed, allowing the model to prospectively predict the design maps with high physical fidelity prior to fabrication.

4.3 Parametric design maps for array-oriented optimization

After establishing the reliability of the simulation model and confirming that it reproduces the measured device behavior at the level of key spectral features and correct order of magnitude, we use the relationship between N_1, N_2, and Q as an example to illustrate a reusable simulation driven workflow. The approach is to perform a systematic sweep of the structural parameters on the calibrated model, extract Q using a consistent metric definition and automated post processing, and then summarize the results as a design map that directly links structural choices to performance outcomes.

As shown in Fig. 6, the 3D surface provides an intuitive view of how Q varies across the N_1 and N_2 space, while the heatmap with contour projection facilitates identification of high Q regions and their boundaries. From a physical perspective, the roles of N_1 and N_2 in shaping the resonance are distinct but complementary. The parameter N_1 governs the effective active transduction area of the device. Expanding N_1 not only decreases the radiation resistance and enhances the overall electromechanical coupling efficiency but also significantly enlarges the physical footprint of the interdigital region. For array-oriented olfaction sensors, this expanded active area is highly advantageous; it provides a more accommodating and uniform surface for the subsequent deposition of viscoelastic sensing films, thereby maximizing the gas-interaction interface for future functionalization. Crucially, establishing this rigorously optimized, high Q bare cavity baseline is a methodological prerequisite. It enables the systematic isolation and resolution of acoustic scattering and cavity design constraints prior to introducing the multi-physics complexities inherent to real-world gas detection. By securing this pure electro-acoustic foundation first, subsequent phases—such as rigorous S_{21} curve calibration and mass loading experiments on actual sensor batches—can be executed with minimized geometric interference. Conversely, the parameter N_2 dictates the confinement strength of the acoustic cavity. Increasing N_2 enhances the Bragg reflection at the gratings, which effectively traps more acoustic energy within the resonant cavity and minimizes longitudinal acoustic leakage. This robust cavity feedback directly contributes to the elevation of the Q factor. However, as depicted in the design maps, increasing either parameter eventually leads to diminishing returns, suggesting a saturation-like behavior where further additions provide minimal incremental acoustic confinement but consume valuable chip real estate. Importantly, high Q is not exclusive to the combination of simultaneously large N_1 and large N_2. Elevated Q can also be achieved with combinations of high N_1 and low N_2, as well as high N_2 and low N_1. This observation is practically useful when the available device area is constrained. When the reflector length is limited, prioritizing a larger N_1 can help maintain a high Q while simultaneously offering a larger sensing area. Conversely, when the IDT region is area-limited, increasing N_2 can compensate by strengthening cavity feedback.

5. Conclusions

This study establishes a comprehensive MA-FEM workflow to optimize resonant Rayleigh wave SAW devices. By integrating stable computational boundaries, phenomenological loss calibration, and an external lumped-element loading network, the model successfully bridges the gap between idealized simulations and experimental transmission spectra. Utilizing this validated framework, parametric design maps were constructed to quantify how the number of IDT pairs and reflector strips jointly shape the quality factor. Experimental validations confirmed these trends, demonstrating that optimal cavity feedback and expanded active areas can be strategically balanced under footprint constraints for array-oriented implementations.

Despite its predictive advantages, the proposed methodology inherently faces limitations rooted in physical manufacturing tolerances. The deterministic nature of the MA-FEM assumes ideal geometric fidelity and uniform material properties. Consequently, while the simulation captures macroscopic trends and nominal behaviors reliably, the absolute point-to-point accuracy of the predicted spectra remains bounded by these stochastic fabrication realities. Nevertheless, this work provides a foundational methodology for the intelligent design

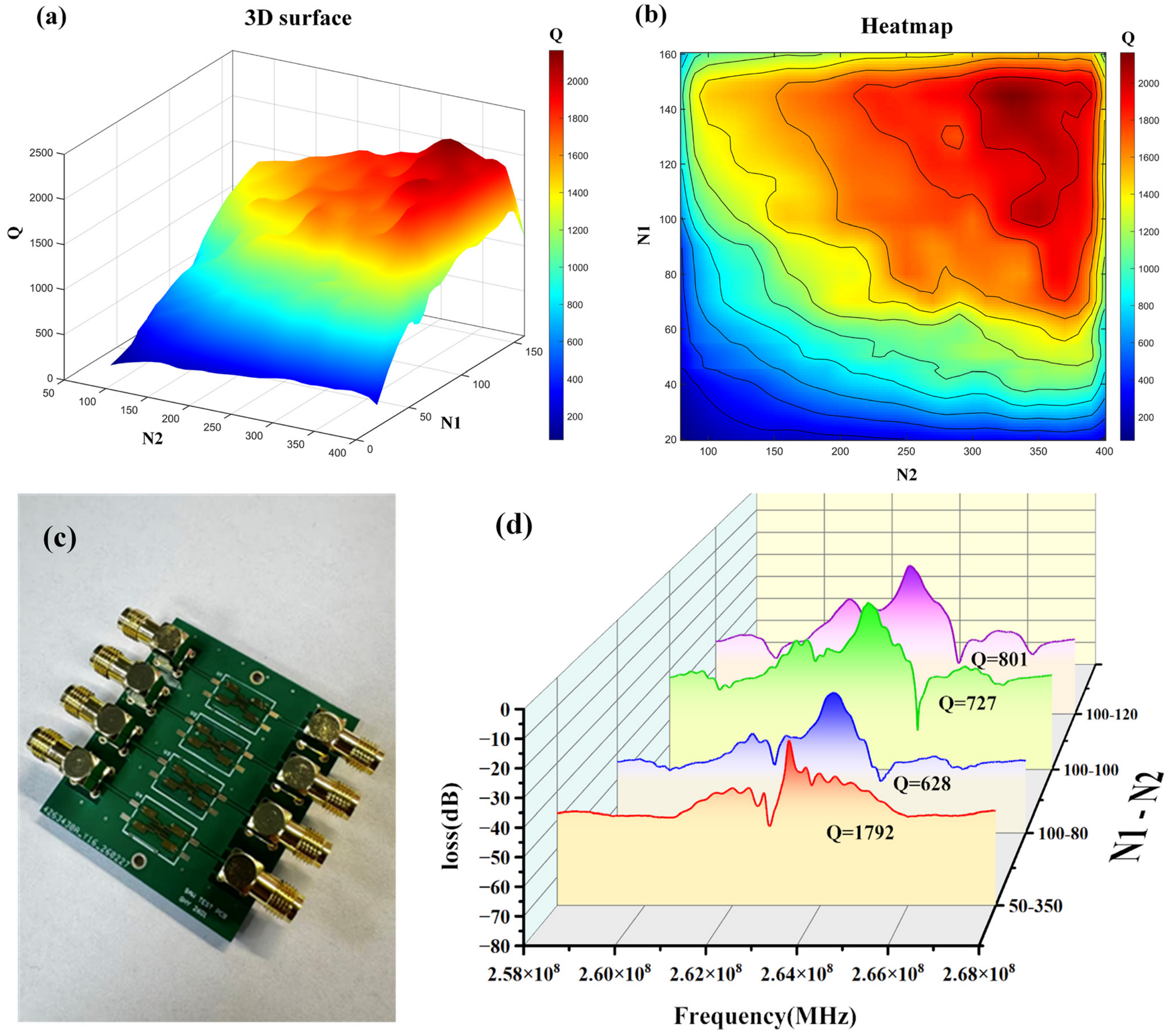

Fig. 6 Parametric design map of the quality factor in the N_1–N_2 space and its experimental validation. (a) 3D surface of extracted Q as a function of the number of IDT electrode pairs N_1 and the number of reflector strips per side N_2. (b) Corresponding heatmap with contour overlay, illustrating performance gradients and high Q design regions. (c) Photograph of the fabricated array-oriented testbed supporting four distinct (chip 1–4, corresponding to configurations 100–80, 100–100, 100–120, and 50–350). (d) Measured S_{21} transmission spectra and extracted Q factors for the four devices, confirming that optimal cavity feedback and expanded active areas can be strategically balanced under footprint constraints.

of SAW olfaction sensors. By transitioning from a traditional fabrication trial-and-error loop to a physics-anchored, simulation-driven paradigm, the MA-FEM workflow significantly narrows the screening space for high-performance prototypes. More importantly, this methodology furnishes the fundamental platform required for the next phase of experimental implementation. By validating the bare device architecture first, it ensures that upcoming performance evaluations—specifically S_{21} curve calibrations and targeted mass loading experiments on newly processed sensor arrays—are built upon a structurally optimized acoustic foundation. Looking forward, as the development of biomimetic sensing arrays increasingly relies on data intelligence, this modeling pipeline can be leveraged to generate extensive, high-fidelity virtual datasets. Such digital-twin approaches will ultimately empower machine learning models to perform rapid performance prediction, robustness analysis under manufacturing variations, and inverse structural design, accelerating the large-scale deployment of next-generation smart sensor arrays.

Author contributions

Hongyang Guo: writing – original draft, software, visualization, investigation. Xiaojing Zhang: formal analysis. Xinxin Li: resources. Ping Wang: supervision. Hao Jia: methodology. Liujing Zhuang: project administration.

Conflicts of interest

All authors declare that they have no known competing financial interests or personal relationships that could have appeared to influence the work reported in this paper.

Data availability

The data that support the findings of this study are available from the corresponding author upon reasonable request.

Acknowledgements

This work was supported by the National Key Research and Development Program of China (2024YFB3212300), National Natural Science Foundation of China (62120106004), and the Fundamental Research Funds for the Central Universities (226-2025-00037).

References

1 T. Zhou, J. Ma, Z. He, C. He, X. Zhang, X. Wu, H. Li, X. Xie, L. Chen and X. Chen, *RSC Adv.*, 2025, **15**, 45359–45375.
2 I. Di Filippo, Z. Anfar, G. Magna, P. Pranee, D. Monti, M. Stefanelli, R. Oda, C. Di Natale and R. Paolesse, *Nanoscale Adv.*, 2024, **6**, 4470–4478.
3 Q. Yang, B. Cui, J. Jin, L. Cheng, X. Xue, Y. Yin and W. Wang, *Sens. Int.*, 2026, **7**, 100348.
4 H. Zhou, S. G. Ramaraj, K. Ma, M. S. Sarker, Z. Liao, S. Tang, H. Yamahara and H. Tabata, *Nanoscale Adv.*, 2023, **5**, 6999–7008.
5 A. O. Ghoname, L. Gao, A. E. Hassanien and S. Gong, *Sens. Actuators, A*, 2025, **394**, 116963.
6 Y. Li, X. Wei, Y. Zhou, J. Wang and R. You, *Microsyst. Nanoeng.*, 2023, **9**, 129.
7 A. Hu, S. Zhai, B. Cui, Y. Yin, C. Zhang, W. Wang and Y. Pan, *IEEE Trans. Instrum. Meas.*, 2025, **74**, 1–12.
8 T. Zhou, A. Reinhardt, M. Bousquet, J. Eymery, S. Leake, M. V. Holt, P. G. Evans and T. Schülli, *Nat. Commun.*, 2025, **16**, 2822.
9 C. Tu, T.-y. Zhang, Z. Zhang, Q.-w. Huang and X.-s. Zhang, *J. Micromech. Microeng.*, 2024, **34**, 045007.
10 Z. Ji, J. Zhou, Y. Guo, Y. Xia, A. Abkar, D. Liang and Y. Fu, *Microsyst. Nanoeng.*, 2024, **10**, 94.
11 S. Li, *J. Appl. Phys.*, 1996, **80**, 5264–5269.
12 B. Cui, W. Wang, L. Cheng, J. Jin, A. Hu, Z. Ren, X. Xue and Y. Liang, *Commun. Eng.*, 2025, **4**, 15.
13 X. Zhang, L. S. Wong, Z. Tang, H. Xiong, J. Sun, L. Kong, M. Tu, Y. Hu, Y. Zhou, W. Zhu, K. J. Hsia, H. Wan and P. Wang, *ACS Sens.*, 2025, **10**, 2994–3002.
14 Z. Shen, H. Liu, H. Qi, X. Liu, H. Li, M. Li and H. Li, *Sens. Actuators, B*, 2025, **444**, 138341.
15 D. Mandal and S. Banerjee, *Sensors*, 2022, **22**, 820.
16 K. F. Young and H. P. R. Frederikse, *J. Phys. Chem. Ref. Data*, 1973, **2**, 313–410.
17 Y. Wang, M. K. Chyu and Q.-M. Wang, *Sens. Actuators, A*, 2014, **220**, 34–44.
18 D. Morgan, *Surface Acoustic Wave Filters: With Applications to Electronic Communications and Signal Processing*, Academic Press, Oxford, UK, 2nd edn, 2007.
19 X. Wang, P. Li and F. Jin, *Appl. Math. Model.*, 2019, **75**, 101–115.
20 Y.-C. Lee and S. H. Kuo, *Sens. Actuators, A*, 2001, **94**, 129–135.
21 H. Xu, S. Fu, R. Su, J. Shen, F. Zeng, C. Song and F. Pan, *Appl. Sci.*, 2021, **11**, 6383.
22 M. J. A. Schuetz, E. M. Kessler, G. Giedke, L. M. K. Vandersypen, M. D. Lukin and J. I. Cirac, *Phys. Rev. X*, 2015, **5**, 031031.
23 Q. Lin, C. Zhao, M. Li and H. Xu, *Chemosensors*, 2024, **12**, 255.
24 K. Bodenhöfer, A. Hierlemann, G. Noetzel, U. Weimar and W. Göpel, *Anal. Chem.*, 1996, **68**, 2210–2218.
25 M. M. Memon, Q. Liu, A. Manthar, T. Wang and W. Zhang, *Micromachines*, 2023, **14**, 945.
26 X. Chen, Y. Li, C. Pan, S. Weng, X. Xie, B. Zhou, H. Dong and D. Zhu, *Anal. Chem.*, 2025, **97**, 12633–12641.
27 M. Dorrestijn, A. Bietsch, T. Açıkalın, A. Raman, M. Hegner, E. Meyer and C. Gerber, *Phys. Rev. Lett.*, 2007, **98**, 026102.
28 M. Imboden and P. Mohanty, *Phys. Rep.*, 2014, **534**, 89–146.
29 A. Draper, N. McKibben, D. Estrada and Z. Deng, *Sens. Actuators, A*, 2023, **359**, 114491.
30 S. Joshi, S. Hung and S. Vengallatore, *EPJ Tech. Instrum.*, 2014, **1**, 5.
31 D. Mencarelli, B. Djafari-Rouhani, Y. Pennec, A. Pitanti, S. Zanotto, M. Stocchi and L. Pierantoni, *Sci. Rep.*, 2018, **8**, 9256.
32 X. Ma, H. Lei, P. Cai and X. Ji, *Appl. Sci.*, 2022, **12**, 4547.
33 Z. Chen, Q. Zhang, S. Fu, X. Wang, X. Qiu and H. Wu, *Micromachines*, 2021, **12**, 5.
34 M. Radojković, G. Gugliandolo, M. Latino, Z. Marinković, G. Crupi and N. Donato, *Micromachines*, 2023, **14**, 967.
35 G. Gugliandolo, Z. Marinković, G. Campobello, G. Crupi and N. Donato, *Micromachines*, 2021, **12**, 303.
36 M. A. N. Alper ŞİŞ, *Int. J. Adv. Eng. Pure Sci.*, 2024, **36**, 59–69.